Entropy-stabilized materials as a platform to explore terbium-based pyrochlore frustrated magnets

Florianne Vayer, Sylvain Petit, Françoise Damay, Jan Embs, Stéphane Rols, Claire Colin, Elsa Lhotel, Dalila Bounoua, Nita Dragoe, David Bérardan, et al.

Entropy-stabilized materials as a novel platform to explore frustrated magnetic systems : the case of $Tb_2(TiZrHfGeSn)_2O_7$

F. Vayer[a], S. Petit[b], F. Damay[b],
J. Embs[c], S. Rols[d], C. Colin[e], E.Lhotel[e], D. Bounoua[b], N. Dragoe[a], D Bérardan[a] and C. Decorse[a]

[a]Université Paris-Saclay, Institut de Chimie Moléculaire et des Matériaux d'Orsay, UMR CNRS 8182, F-91405 Orsay, France
[b]Université Paris-Saclay, Laboratoire Léon Brillouin, CEA-CNRS UMR12, F-91191 Gif-sur-Yvette Cedex, France
[c]Laboratory for Neutron Scattering and Imaging, Paul Scherrer Institut, CH-5232, Villigen, Switzerland
[d]Institut Laue-Langevin, 71 avenue des Martyrs, 38042 Grenoble Cedex 9, France,
[e]Institut Néel, CNRS, Université Grenoble-Alpes, CNRS, F-38042 Grenoble, France

Version : 6 November 2024

Correspondence to : sylvain.petit@cea.fr, claudia.decorse@universite-paris-saclay.fr

ABSTRACT

In this work, we take advantage of the intrinsic disorder of the entropy-stabilized compound $Tb_2(TiZrHfGeSn)_2O_7$ to investigate the elusive ground state of Tb-based pyrochlore magnets. Extensive characterizations were performed using X-ray and neutron scattering, as well as magnetization and specific heat measurements. No long range magnetic order is observed yet magnetic diffuse scattering is present, and is characteristic of antiferromagnetic first-neighbour correlations. The crystal field excitation spectrum visibly reflects the smooth environmental disorder of the Tb environment, with very broaden levels in a large energy range. The low energy dynamics, however, are characterized by a narrow mode at about 0.4 meV, consistent with specific heat. Modelling of the crystal field excitations, including isotropic random shift δ of the oxygen positions around Tb sites, accounts reasonably well with those experimental results. Remarkably, this modelling points out that the spectral weight of the 0.4 meV mode is a direct consequence of deviations from the D_{3d} symmetry of the Tb environment. It especially

increases as δ increases. In the light of these results, quadrupolar interactions are also discussed, emphasizing the potential of the high entropy approach to achieve exotic phases in Tb pyrochlores, thanks to a delicate tuning of smoothen disorder.

INTRODUCTION

The concept of high-entropy stabilization has had a major impact in material research over the past few years, as it offers the possibility in alloys and oxides to stabilize new single phase materials from multiple constituting elements, whose simultaneous solubility is enhanced by the large configurational entropy [1], [2], [3]. Although locally randomly chemically disordered, these high-entropy materials exhibit long-range structural order, and their properties can be optimized through a careful selection of their constituting elements : a variety of research fields has thus recently benefited from high-entropy stabilized materials with enhanced chemical or physical properties, such as thermoelectricity [4], catalysis [5], superionic conductivity [6] or energy storage [7], with crystal structures including rock-salt, fluorite, or perovskite structures, for instance.

Very recently, the first entropy-stabilized pyrochlores were discovered [1], [2], bringing the possibility to prepare pyrochlore compounds in which the B site is randomly occupied by five different tetravalent cations, and thereby expanding the use of stabilized entropy compounds to the fundamental physics of frustrated magnetism [8] [9] [10].

We apply it here to the understanding of the elusive ground state of $Tb_2Ti_2O_7$, a Coulomb phase which remains an enigma to this day [11]. A Coulomb phase is a new state of matter without conventional long-range order, but in which magnetic configurations belonging to the ground state are built following a local organizing principle. The best-known and best-understood example are spin ices $Ho_2Ti_2O_7$ and $Dy_2Ti_2O_7$: the organizing principle is known as the "ice rule" and selects “2-in, 2-out” configurations of the spins in any rare-earth tetrahedron, to form, at the classical level, an extensive set of degenerate ground states, with a non-zero residual entropy at low temperature [12], [13], [14], [15]. In $Tb_2Ti_2O_7$, the picture is made more complex because of the potentially major role played by the interactions between the quadrupolar moments carried by the 4f electronic density of the Tb ions [16], [17], [18], [19], [20], [21], [22], [23], [24], [25] [26]. In particular, the low energy and low temperature magnetic excitation spectrum of $Tb_2Ti_2O_7$ encompasses a mode around 0.3 meV with substantial spectral weight [20], which, given the non-Kramers character of Tb^{3+}, implies a deviation away from the D_{3d} local symmetry of the rare earth site (derived from the space group), arguably induced by quadrupole-quadrupole interactions.

Disorder is of particular interest in the case of Tb based pyrochlores (and more generally for non-Kramers ion like Tb or Pr [27] [28] [29] [30] [31] [32]), as it tends to modify locally the

electronic density and thus to perturb or even conceal quadrupolar interactions. This property can then be used to get a better understanding of the intricacies of the $Tb_2Ti_2O_7$ ground state, and of Coulomb [33] [34] [35] phases more generally. In terbium pyrochlores, the influence of B-site charge distribution disorder has been investigated in Tb_2ScNbO_7 [36], and that of interstitial oxygen in $Tb_2Hf_2O_7$ [37].

We report here a comprehensive study of the effect of the smooth disorder provided by entropy-stabilization in the terbium pyrochlore $Tb_2(Ti_{0.2}Zr_{0.2}Hf_{0.2}Ge_{0.2}Sn_{0.2})_2O_7$ (also labelled $Tb_2(TiZrHfGeSn)_2O_7$ or abbreviated as TbMOX thereafter). Diffraction experiments in TbMOX first confirm that the pyrochlore *Fd*-3*m* crystal structure is preserved. Below 10 K, magnetic correlations develop, giving rise to a magnetic diffuse scattering signal similar to that of $Tb_2Ti_2O_7$ and suggesting like in the latter the existence of significant antiferromagnetic interactions between nearest neighbours. The crystal field excitation spectrum of TbMOX is characterized by several very broad levels between 4 and ~ 40 meV. At lower energies, a quasielastic mode is observed, which transforms, below 1.5 K, into a nearly flat inelastic mode located around 0.4 meV, as in $Tb_2Ti_2O_7$. Strikingly, the energy width of this level remains narrow, in contrast with the broadened higher energy crystal field excitations. The spectral weight of the 0.4 meV mode is also slightly modulated with respect to momentum transfer, as expected in the case of a local, rather than long range, magnetic order.

To interpret those experimental observations, we propose a scenario in which the B site compositional disorder induces random shifts (δ) of the oxygen atoms, directly impacting the crystal electric field (CF) Hamiltonian. Numerical calculations show that the Tb magnetic moment amplitude is actually not strongly affected by disorder, which could explain why magnetic interactions and correlations are similar within Tb pyrochlores, whether disordered or not, such as $Tb_2Ti_2O_7$, TbMOX, Tb_2ScNbO_7, $Tb_2Nb_2O_7$ or $Tb_2Hf_2O_7$. Furthermore, calculations indicate that oxygen shifts, not only broaden the CF levels considerably, but also contribute significantly to the intensity of the low energy mode, as expected for non-Kramers ions like Tb^{3+}, since they correspond to local deviations from the D_{3d} symmetry. The relative strengths of disorder and quadrupolar interactions with respect to magnetic couplings in TbMOX is discussed in the framework of recent theories on quantum spin liquids.

EXPERIMENTAL METHODS

Synthesis. A powder sample of $Tb_2(Ti_{0.2}Zr_{0.2}Hf_{0.2}Ge_{0.2}Sn_{0.2})_2O_7$ (TbMOX) was prepared by mixing TiO_2, ZrO_2, HfO_2, GeO_2 and SnO_2 with Tb_4O_7 in stoichiometric amounts. The mixture was then heated up to 1200°C for 12 hours to avoid any Sn loss [38], [39]. After an intermediate grinding, a second thermal treatment at 1600°C for 15 hours was carried out. During this last step, platinum foil was used to prevent any contamination from the alumina crucible. The pyrochlore phase forms during this second step and, being entropy stabilized, is preserved by quenching to room temperature (RT) [1]. More detailed chemical characterizations are shown on Figure S5 of ref. [1]. Reproducibility between different sample batches was ensured by keeping strict synthesis steps. Comparing the physical properties (specific heat, magnetization) of different batches of the same composition confirmed the reproducibility of the synthesis process.

X-ray diffraction experiments. The room temperature structure was characterized with a laboratory powder X-ray diffractometer (Panalytical X'Pert, $K\alpha_1$ radiation), equipped with a fast detector X'celerator. It confirmed that the sample was single phase and of high crystalline quality.

Neutron powder diffraction (NPD) experiments were carried out on the CRG-D1B neutron diffractometer (λ = 1.28 Å and λ = 2.52 Å), at the ILL facility, equipped with a dilution fridge, on a m = 5 g. sample. Rietveld analysis of the X-ray and neutron diffraction data were performed with the Fullprof software [40].

Inelastic neutron scattering experiments were carried out on the thermal time-of-flight instrument Panther at ILL, between 10 K and 200 K in an orange cryostat, at various incident energies (E_i = 130, 50 and 30 meV). Complementary experiments were carried out at SINQ on the cold time-of-flight spectrometer Focus, in a dilution fridge environment from 50 mK to 100 K. The sample was introduced in a double wall copper sample holder. The wavelength of incident neutrons was λ = 5.0 Å [41] and provided an energy resolution of 70 µeV.

A high temperature spectrum (100 K) was first measured to serve as reference. The very low energy spectrum of TbMOX encompasses a quasielastic contribution strongly amplified by the detailed balance factor at 100 K, so that the 100 K reference cannot be used for subtraction directly. To correct from temperature effects, the 100 K spectrum was thus first reduced to a series of energy scans, for a number of Q positions between 0.25 and 2.85 $Å^{-1}$. Each scan $I_{exp}(Q,\omega)$ was then fitted in a small energy interval $-\omega_1 < \omega < \omega_1, \omega_1 \approx 0.1\, meV$ to a function consisting in a Lorentzian on top a Gaussian profile :

$$I_{model} = I_o\, e^{-4\log 2\left(\frac{\omega}{\sigma}\right)^2} + \left(1+\frac{1}{e^{\omega/T}-1}\right)\frac{A}{T}\frac{\omega}{\omega^2+\gamma^2} \quad (2)$$

The Gaussian and Lorentzian contributions represent the elastic and quasielastic response respectively. We then used the quantity $s(Q,\omega) = I_{exp}(Q,\omega,T=100K) - \left(1+\frac{1}{e^{\omega/T}-1}\right)\frac{A}{T}\frac{\omega}{\omega^2+\gamma^2}$ to serve as the proper background reference, which we used for subtraction on the spectra taken at 0.05, 0.5, 1.2 and 5 K.

Magnetization measurements were carried out using the VSM option of a Dynacool PPMS (Quantum Design), from 1.5 to 50 K, and up to 8 T. Complementary magnetization measurements in 100 Oe were also performed down to 500 mK, on a MPMS magnetometer (Quantum Design) equipped with a ^{3}He insert, at the LPS characterization platform (Orsay, France). Low temperature magnetization and ac susceptibility measurements were also performed between 70 mK and 4.2 K on a magnetometer equipped with a ^{3}He-^{4}He dilution refrigerator developed at the Institut Néel CNRS. The sample was a sintered parallelepipedic pellet of 10.14 mg.

Specific heat measurements (C_p) were performed on a PPMS (Quantum Design) equipped with a ^{3}He insert at the Institut Néel, on a sintered pellet (m = 9.98 mg). To estimate the phonon contribution C_{ph} to C_p, an yttrium based sample ($Y_2(Ti_{0.205}Zr_{0.205}Hf_{0.205}Ge_{0.180}Sn_{0.205})_2O_7$, *m* = 6.18 mg (YMOX)) was also measured as reference. The mass difference between Y and Tb was taken into account by introducing an additional T/r correction, which allows one to estimate C_{ph} (T) = $C_{tot,YMOX}$ (T/r_M) with r_M = (M_{YMOX}/M_{TbMOX})$^{0.5}$ (M : molar mass). A ^{159}Tb nucleus hyperfine structure correction (C_N) was also applied to account for the increasing C_p at low temperature [42], using a Schottky anomaly approximation, with the same gap value as reported for $Tb_2Ti_2O_7$ (Δ_{Tb} ~ 0.1 K, [43]). The magnetic specific heat is then calculated as C_{mag} (T) = $C_{tot,TbMOX}$ (T) – C_{ph} (T) - C_N (T).

EXPERIMENTAL RESULTS

Crystal structure of TbMOX at room temperature

Laboratory X-ray and neutron powder diffraction data confirm that TbMOX has a *Fd*-3*m* pyrochlore structure, with *a* = 10.3287(10) Å at room temperature (RT) (Figure 1). The Bragg peak width is resolution limited, and there is no evidence of diffuse scattering in either of the diffractograms. Rietveld refinements of the structure confirm the $Tb_2M_2O_7$ stoichiometry of the

sample, with M corresponding to equal amounts of Ti, Zr, Hf, Ge, Sn. The only refinable atomic position is 48f O (*x*, 0.125, 0.125) with x = 0.3338(1). Isotropic thermal displacements are large for all atoms, reflecting the impact of the size disorder on the pyrochlore B site (B_{Tb} = 0.90(6) Å^2, B_M = 0.52(10) Å^2, B_{O_8b} = 0.38(12) Å^2, B_{O_48f} = 1.27(6) Å^2 at 300 K). Some anti-site disorder (corresponding to cross substitutions between the RE and B sites) is not to be fully discarded however, as the neutron scattering length of Tb (b_{coh}(Tb) = 7.38 fm) is close to that of Hf (b_{coh}(Hf) = 7.7 fm) and Zr (b_{coh}(Zr) = 7.16 fm) [44]. Note that such defects have not been evidenced in $Tb_2Hf_2O_7$ [37]. Within the resolution of the neutron diffraction experiments, the crystal structure remains cubic down to 1.5 K.

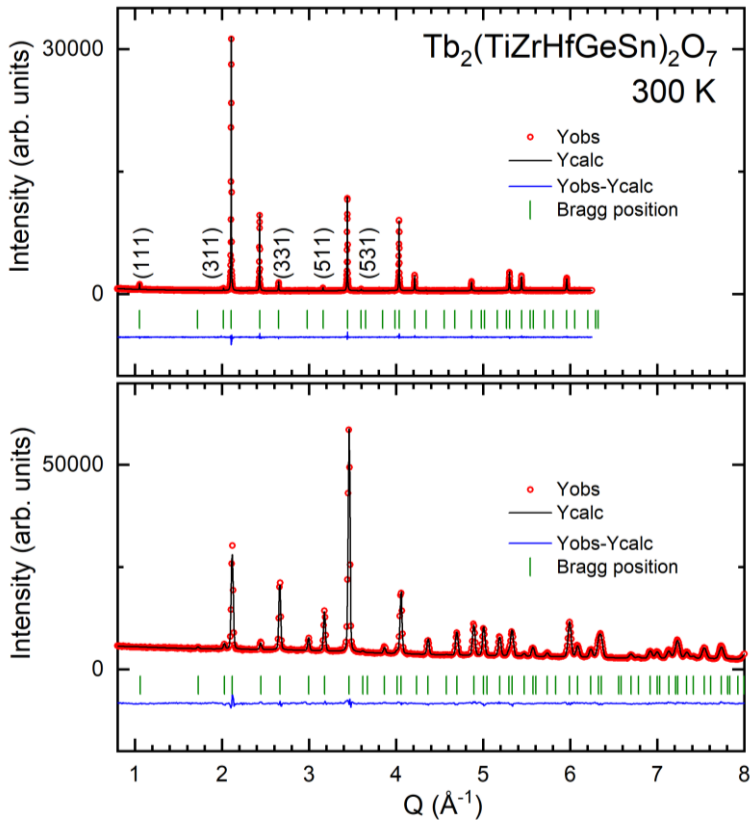

Figure 1. Rietveld analysis of the X-ray (top) and neutron diffractograms (bottom) of pyrochlore TbMOX at room temperature. Bragg peaks characteristic of the pyrochlore crystal structure (with respect to fluorite) are indexed.

Macroscopic magnetic characterizations

No ordering is observed in the magnetization curve of TbMOX, down to 2 K, as shown in Figure 2a. The inverse susceptibility shows an almost linear behavior above 20 K, as previously observed in other Tb based pyrochlores [11] [36] [37] [45] [46]. A fit to a Curie-Weiss law gives an effective moment of 9.5 μ_B, in agreement with the theoretical value expected for the

free Tb^{3+} ion ($g_J J = 9\ \mu_B$). The obtained Curie-Weiss temperature is θ_{CW} = -6.4 K, comparable with the value obtained in Tb_2ScNbO_7 [36] but smaller, in absolute value, than in pure $Tb_2Ti_2O_7$ [47]. Because of CF effects, however, θ_{CW} should be corrected, a first approximation being to write it as a sum of two contributions, one due to exchange θ_o, the other due to the CF splitting: $\theta_{CW} = \theta_o + \theta_{CW}^{CF}$. According to [47], the CF contribution θ_{CW}^{CF} is about −6 K, hence $\theta_o \sim$ -0.5 K in TbMOX, pointing to weak effective antiferromagnetic interactions.

Nevertheless, as previously shown in [47], this Curie-Weiss temperature is strongly affected by crystal field effects and thus is not directly related to the sign of the magnetic interactions. This is all the truer in the presence of disorder in the Tb^{3+} ions surroundings [36]. The isothermal magnetization curve as a function of magnetic field measured at 70 mK does not saturate up to the highest measured field of 8 T (see Figure 2b). Magnetization reaches a value of 4.75 μ_B/Tb at 8 T, almost similar to observations in $Tb_2Ti_2O_7$ ([45] [48] [46] [49] [Tb2Nb2O7]), indicating the same magnetic state for the Tb^{3+} ions.

Zero Field Cooled - Field Cooled measurements performed below 4 K in low magnetic field exhibit a maximum around 0.65 K, while a separation between the two curves is observed below about 0.8 K (see Figure 2d). When increasing the field, the maximum broadens and slightly shifts to higher temperatures while the temperature at which the irreversibility appears decreases. The irreversibility is totally suppressed at 5000 Oe. This behavior is reminiscent of previous observations on Tb based pyrochlores and indicates a spin freezing, which can be characterized by the frozen spins ratio $r = 1\text{-}M_{ZFC}/M_{FC}$. In the smallest magnetic field applied in this study (H = 36 Oe), r is about 50 %, a value comparable to the one observed in Tb_2ScNbO_7 [36] at the same temperature. To further probe this effect and determine the existence of a possible spin-glass transition, *ac* susceptibility measurements were performed. A frequency dependence is observed in χ' and χ'' as shown in Figure 2c, which could not be described by an Arrhenius law. On the other hand, the dependence of the χ' maximum could satisfactorily be described by a scaling law $\tau = \tau_0\ ((T\text{-}T_g)/T_g)^{-z\nu}$ with $\tau_0 = 2.10^{-7} \pm 5.10^{-8}$ s, $T_g = 0.675 \pm 0.05$ K and $z\nu = 5 \pm 1$. Measurements in an extended frequency range would be necessary to better refine these parameters, but they are in the same range as the ones obtained for other disordered Tb pyrochlores compounds in which a spin-glass transition has been reported, namely $Tb_2Hf_2O_7$ [37] and Tb_2ScNbO_7 [36].

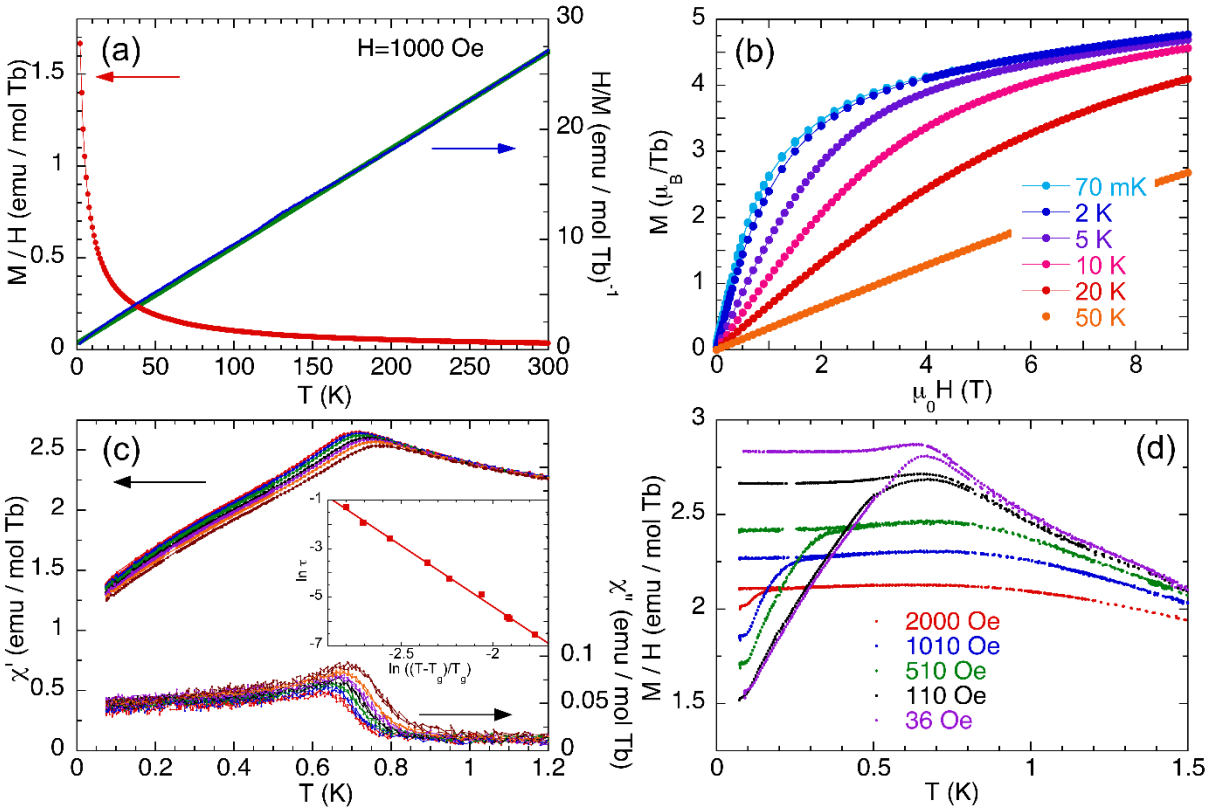

Figure 2. (a) TbMOX magnetization divided by the field M/H (left, red points) and its inverse H/M (right, blue points) versus temperature. The green line is a linear fit: H/M = 0.567 + 0.088 T. (b) M versus H measured at several temperatures between 70 mK and 50 K. (c) TbMOX *ac* susceptibility χ' (left) and χ'' (right) versus T measured in an alternative field of 2.3 Oe at several frequencies *f* between 0.57 Hz and 57 Hz. Inset: lnτ versus ln((T-T_g)/T_g) with T_g = 0.675 mK and T the temperature of the χ' maximum at a given frequency $f = 1/2\ \pi\tau$. The line is a linear fit: $\ln\tau = -15.4 - 5.0\ \ln((T-T_g)/T_g)$. (d) ZFC-FC magnetization M/H of TbMOX vs. T at several magnetic fields between 36 Oe and 2000 Oe.

Low temperature neutron diffraction

Neutron powder diffraction experiments carried out down to 50 mK and up to 40 K indicate that TbMOX does not show any long-range magnetic ordering (Figure 3) in that temperature range.

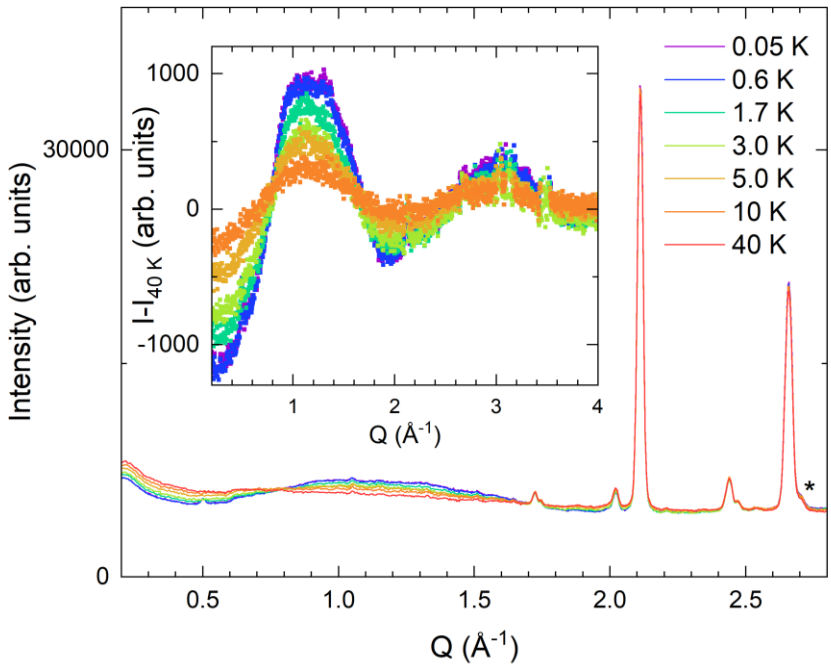

Figure 3. Evolution with temperature of the neutron powder diffractograms of TbMOX. The Bragg peak labeled with * corresponds to Al. A magnetic impurity appearing below 600 mK is visible around Q = 0.5 Å^{-1}. It cannot be matched with either Tb_2O_3 or Tb_4O_9. Inset: corresponding evolution with temperature of the difference I-I(40K) (same temperature color scheme). The data points corresponding to Bragg positions have been removed for clarity.

The neutron powder diffractograms show however a diffuse scattering signal, more clearly seen on the difference $I\text{-}I_{40K}$ (inset of Figure 3). A basic description in terms of correlated spins was used, introducing correlations up to third-neighbor (that is, up to 7.3 Å):

$$I_M = N\left(\frac{\gamma r_0}{2}\right)^2\left(\rho_0 + \sum_{j,j\neq i}\rho_j\,\frac{\sin(Qd_j)}{Qd_j}\right) \qquad (1)$$

and simply derived from the powder averaged classical expression of the neutron cross section. $\rho_0 = \langle S_i^2\rangle$ is a constant contribution (independent of Q) and represents the square of the average local Tb^{3+} moment. The $\rho_j = \frac{1}{N}\sum_i\langle S_iS_j\rangle$ parameters are associated with Q-dependent contributions and give information on the amplitude and sign of the correlations between neighbouring moments. The sum running over the layers of successive neighbors involves the distances d_j between first, second, up to third neighbors. The d_j (in Å) derived from the cell parameter are d_1 = 3.769, d_2= 6.528, d_3= 7.538. How to derive the normalization factor N is detailed in Appendix. A fitting of the difference curve $I\text{-}I_{40K}$ to this model is shown in Figure 4a, the general shape of the diffuse scattering signal being reproduced quite convincingly. In particular, the bump around 1.1 Å^{-1} is typical of liquid-like correlations between nearest

neighbors. The corresponding temperature evolution of the $\sqrt{\rho_i}$ parameters, shown in Figure 4b represents how the "correlated" moment (in μ_B), embedded in those close-neighbour correlations, develop on cooling from 40 K down to 50 mK.

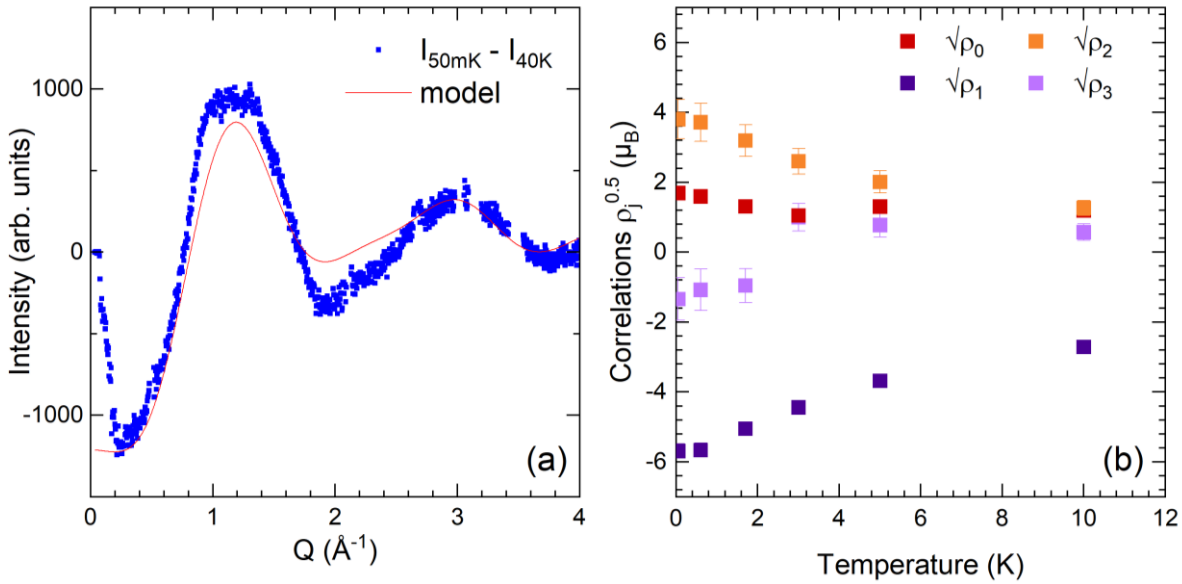

Figure 4. (a) Best fit to the magnetic diffuse scattering signal ($I_{50\,mK}$-$I_{40\,K}$, experimental data as blue symbols) using a short range order modelling (red line) up to third neighbor (see eq. (1), multiplied by the Tb^{3+} form factor). (b) Evolution of the corresponding ρ_j parameters.

From Figure 4b it can be seen that the local moment derived from $\sqrt{\rho_0}$ slightly increases by about 2 μ_B on cooling. This increase is likely a CF effect: with lowering temperature, the CF excited states become less populated which modifies the magnetic moment. More importantly, the first neighbor correlation ρ_1 is negative, characterizing antiferromagnetic interactions, in agreement with the negative θ_{CW}. The magnetic moment estimated from $\sqrt{|\rho_1|}$, is close to 6 μ_B, out of the maximum of 9 μ_B expected for the free Tb^{3+}ion. ρ_2, on the other hand, is positive, indicating ferromagnetic correlations, with a moment $\sqrt{\rho_2}$ close to 4 μ_B. These features are very similar to those observed in $Tb_2Ti_2O_7$ [11], suggesting that the diffuse scattering (along with its typical pinch points [36]) is preserved in TbMOX despite disorder .

Inelastic neutron scattering experiments and crystal electric field scheme

Inelastic neutron experiments were carried out at several incident energies to study crystal field excitations in a large energy range. Probing CF excitations provides information, not only on the crystal field scheme and therefore on the magnetic properties of the Tb^{3+}, but also on the

impact of oxygen positional disorder on the environment of the Tb^{3+}. Indeed, because of the distribution of environments around the Tb^{3+} resulting from the high-entropy approach, instead of the usual discrete and flat features typical of a CF excitation spectrum, a broad magnetic signal, ranging between 4 and 40 meV, can be observed, with four broad maxima around 6, 13, 17 and 40 meV (see Figure 5). The magnetic nature of this signal is confirmed by the Q dependence of its intensity, i.e, decreasing with Q.

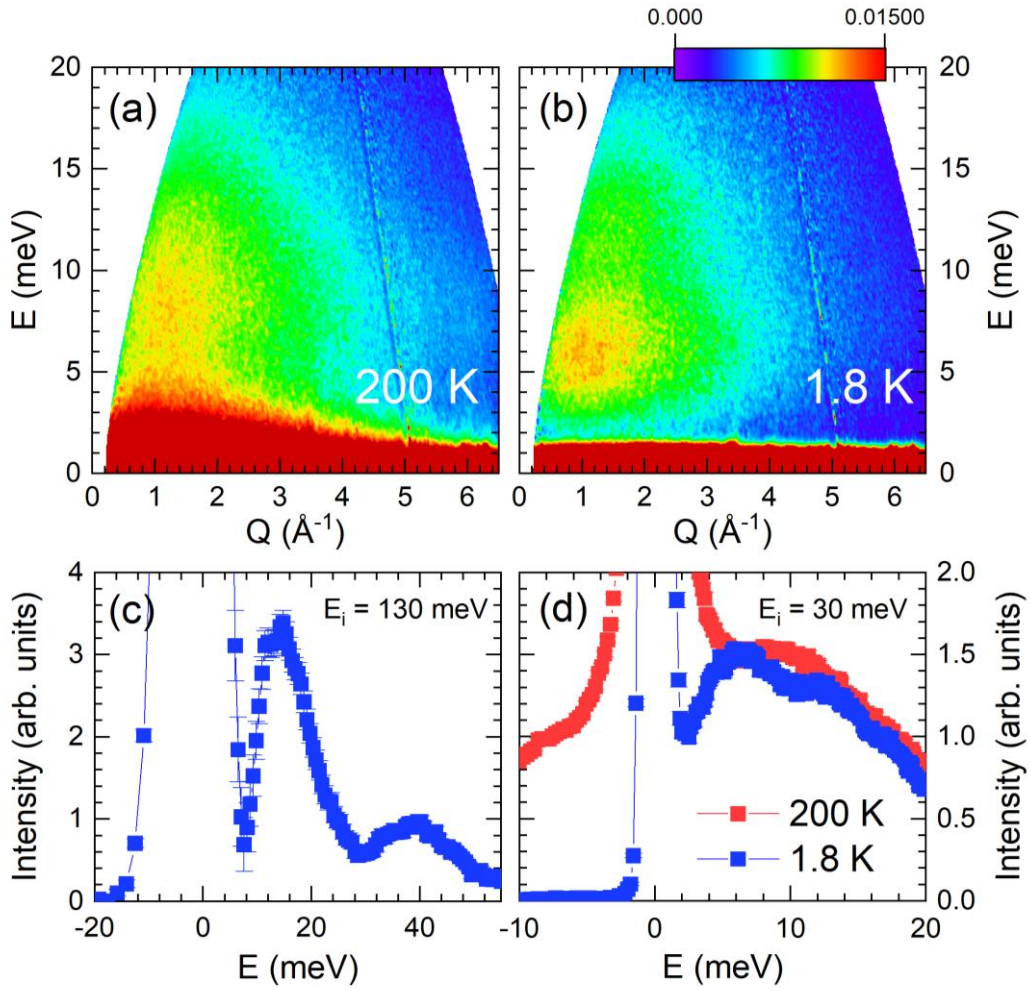

Figure 5. S(Q, E) of TbMOX (E_i = 30 meV) at 200 K (a) and 1.8 K (b). (bc) Integrated (dQ = ± 0.50 Å^{-1}) constant Q = 2.5 Å^{-1} cut at 1.8 K (E_i = 130 meV). (d) Integrated (dQ = ± 0.25 Å^{-1}) constant Q = 2.0 Å^{-1} at 1.8 K and 200 K (E_i = 30 meV).

Additional experiments were then performed down to 50 mK at a smaller incident wavelength (E_i = 3.2 meV, λ=5 Å), as illustrated on Figure 6. The data shown on Figure 6 have been obtained after subtraction of the sample environment intrinsic background (see experimental methods for details). A quasielastic signal is clearly seen on the 5 K excitation spectrum. It transforms, below 1.5 K and down to 50 mK, into an inelastic and nearly flat level at about Δ =

0.37 meV. Strikingly, unlike the higher energy excitations, this level remains quite narrow, with a full width at half maximum of about $\Gamma = 0.25$ meV.

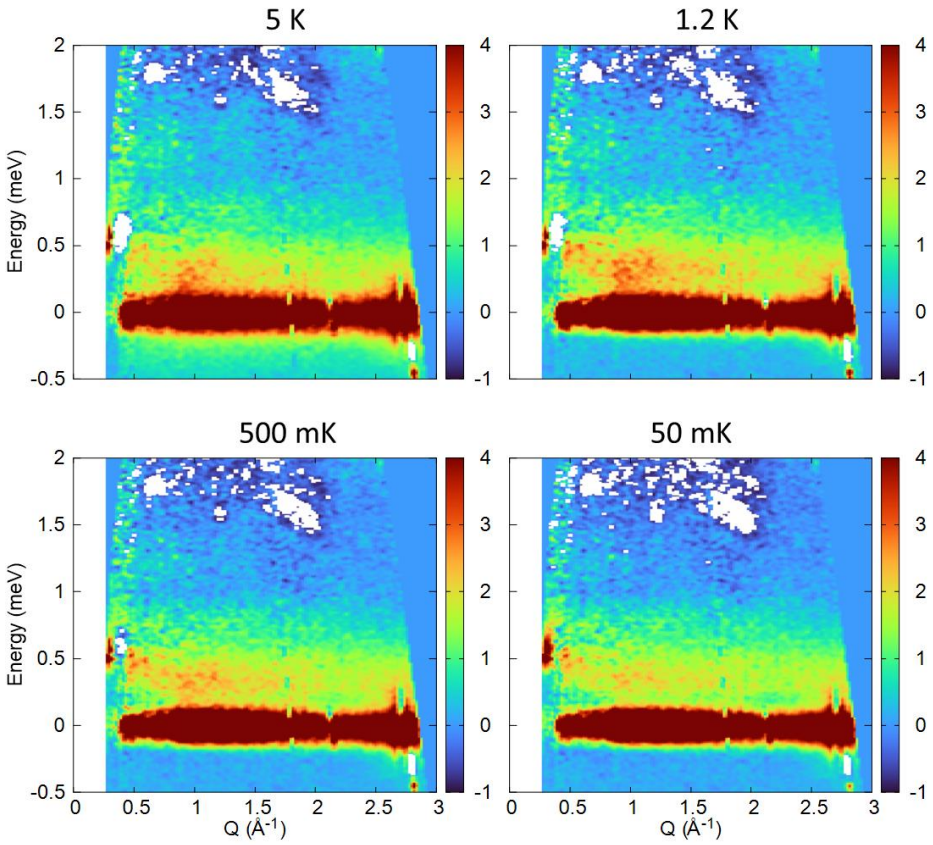

Figure 6. Temperature evolution of the low energy excitation spectrum Q (Q, E) of TbMOX (T = 5, 1.2, 0.5 and 0.05 K). E_i = 3.2 meV. A background has been subtracted (see experimental methods).

Specific heat

Specific heat measurements were performed down to 400 mK. Data shown on Figure 7 are corrected from the phonon contribution, and from the hyperfine contribution of the ^{159}Tb nucleus below 500 mK (see Experimental methods for details). In agreement with the different experiments described previously, no magnetic transition could be detected, the main characteristic of the C_{mag} (T) curve being a broad maximum around 1.8 K. The temperature position of this peak is in good agreement with the existence of the low energy excitation at Δ, a Schottky anomaly being expected at T = 0.4 Δ. Furthermore, since the mean energy of the first crystal field levels in TbMOX is about 6 meV, the specific heat contribution of the latter is expected at high temperature, around 30 K (hence out of the window of this measurement).

This is higher than in $Tb_2Ti_2O_7$ for instance, where it is observed around 6 K [50] [43], but similar to $Tb_2Hf_2O_7$ or Tb_2ScNbO_7 [36].

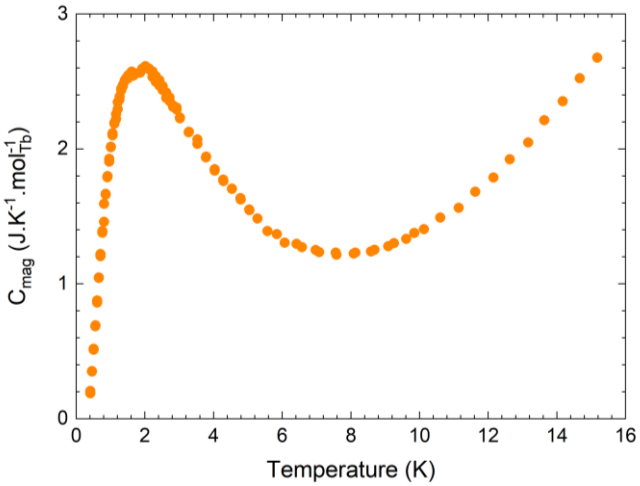

Figure 7. Temperature evolution of the magnetic specific heat of TbMOX after subtraction of the hyperfine and phonon contributions (see experimental methods).

MODELING

Crystal field. A CF scheme is usually modeled by the Hamiltonian

$$H_{CEF} = \sum_{n,m} B_{n,m} O_{n,m} \quad (3)$$

where $B_{n,m}$ are Stevens CF parameters and $O_{n,m}$ are Stevens equivalent operators, written in a $(2J+1)^2$ basis ($J = 6$ for Tb^{3+}). The neutron scattering spectrum writes:

$$S(\omega) = \frac{1}{Z}\sum_{n,m} e^{-\frac{E_n}{T}}\left\{\sum_{a=x,y,z} |< n| I_i^a |m >|^2\right\} \delta(\omega - E_n + E_m) \quad (4)$$

$Z = \sum_n e^{-\frac{E_n}{T}}$ is the partition function, E_n and $|n>$ are the CF energies and wavefunctions, $I_i^{x,y,z}$ denote the three components of the total angular moment. If the symmetry at the rare earth site is the nominal D_{3d}, the Stevens parameters $B_{20}, B_{40}, B_{43}, B_{60}, B_{63}, B_{66}$ should be non-zero. Using published values for $Tb_2Ti_2O_7$, the CF ground state is a doublet, denoted $|\uparrow,\downarrow\rangle$, and characterized by the following properties (non-Kramers character) :

$$\langle\uparrow| I_i^z |\uparrow\rangle = +\mu$$

$$\langle\downarrow|\, I_i^z \,|\downarrow\rangle = -\mu$$

$$\langle\downarrow|\, I_i^{x,y,z} \,|\uparrow\rangle = 0$$

A simple approach to estimate the $B_{n,m}$ is given by the point charge model. In the pyrochlore structure, the environment of a given Tb ion is made of two 8*b* oxygen ions, located symmetrically along the local ⟨111⟩ quantification axis (denoted z hereafter), and six 48*f* oxygen ions, positioned roughly in the basal plane perpendicular to z. To model the influence of the B-site high-entropy, we postulate that oxygen atomic coordinates experience a random isotropic shift δ away from their actual values. Note that in principle, a measure of δ is provided by "thermal displacements" values obtained from the diffraction data. In calculating the $B_{n,m}$, the oxygen positions are then randomly shifted, hence locally breaking the D_{3d} symmetry. All Stevens coefficients are thus now allowed. Sampling the $B_{n,m}$ according to this model, the D_{3d} symmetry is only fulfilled on average, and the inelastic neutron scattering can be evaluated by taking the ensemble average $\bar{S}(\omega)$ over the different random configurations.

Magnetic interactions. The above description is incomplete, however, as the presence of diffuse scattering (Figures 3-4) calls for the existence of magnetic interactions. According to literature [51] [52], and since the three components of the total angular momentum $I_i^{x,y,z}$ do not have cross matrix elements between $\uparrow,\downarrow$ (due to the non-Kramers nature of Tb^{3+} ions), it seems reasonable to consider the following magnetic Hamiltonian:

$$\mathcal{H}_{mag} \approx \sum_{<i,j>} \mathcal{g}^{zz}\, I_i^z\, I_j^z$$

Here the $(+-z)$ coordinates refer to local axes, with z pointing along the local ⟨111⟩ directions and $\mathcal{g}^{zz}$ being the magnetic coupling. To keep our approach simple, we consider a mean field approximation, thus introduce a local molecular field denoted H, so that the total Hamiltonian is :

$$\mathcal{H} \approx \mathcal{H}_{CEF} + H\, I_i^z \qquad (5)$$

Two parameters need then to be determined to model appropriately the neutron data, that is, the molecular field *H* and the standard atomic shift δ. Figure 8 illustrates the results of numerical calculations for different standard shifts δ varying from 0.01 up to 0.1 Å. In these calculations, a constant molecular field $H = 0.45$ K is assumed, leading to a split ground state with a low energy mode at $\Delta \approx 0.4$ meV.

The average inelastic neutron scattering signal $\bar{S}(\omega)$ is shown in Figure 8a. As expected, the CF levels at high energies considerably broaden as δ increases. At low energy, a striking observation is that the spectral weight of the energy mode at Δ is zero if $\delta = 0$; yet, it increases with increasing δ. In other words, the ground state doublet splitting due to the molecular field becomes visible by neutron scattering only if some disorder is present. The energy position Δ is however not strongly affected, which is further corroborated by the temperature evolution of the specific heat shown in Figure 8b. The Schottky anomaly at $T \sim 0.4\ \Delta / k_B \sim 1.8$ K remains essentially unchanged with increasing δ.

At higher temperature, above 8 K, a second maximum tends to develop, due to the series of CF level around 6 meV. It is all the weaker as δ is greater. With disorder, it also widens more and more, as shown in Figure 8b. This widening is due to the random distribution of CF levels in the 6 meV range and to the superposition of their "individual" contributions. The result is a much more spread-out specific heat than when δ is zero.

The histogram illustrating the evolution of the magnetic moment values with δ (Figure 8c) broadens with increasing δ, but remains peaked around $M_z = g_J \langle I_i^z \rangle \approx 7\ \mu_B$, even for standard shifts as large as 0.05 Å. This means a quasi-uniform distribution of the amplitude of local magnetic moments. Despite this rather simple model, all our experimental observations on TbMOX, that is the CF excitations spectrum and the specific heat peak at 1.8 K, can be qualitatively understood.

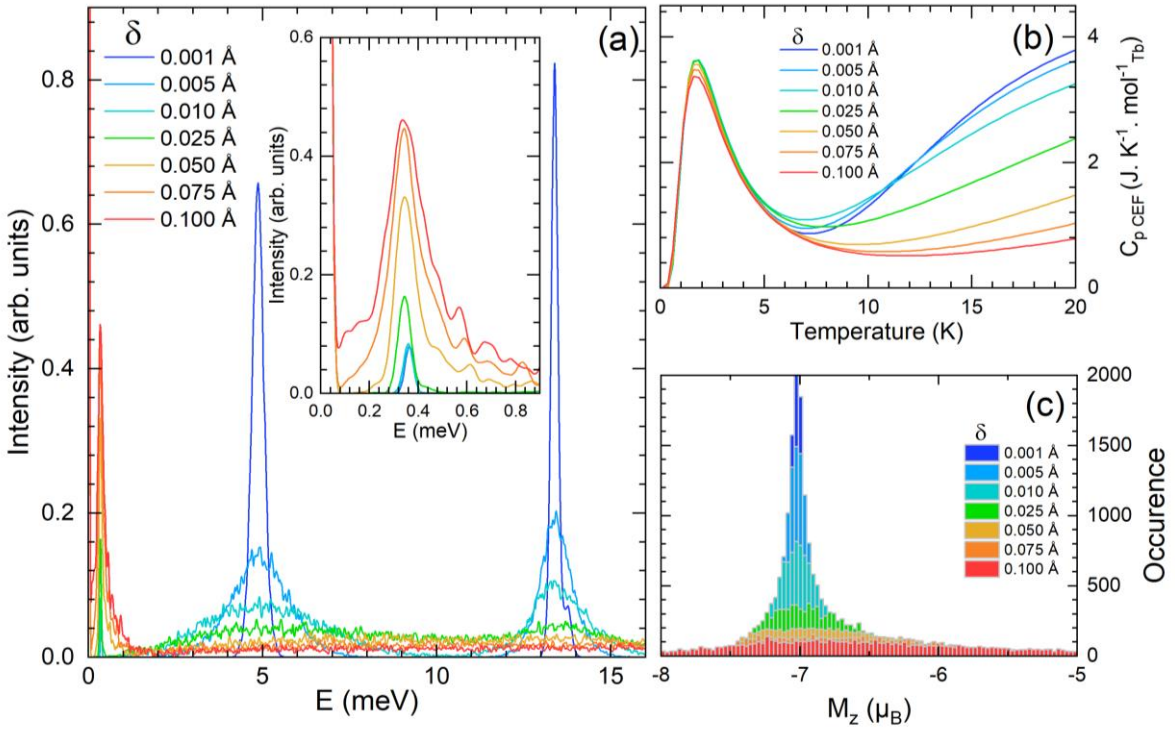

Figure 8. (a) Calculated inelastic neutron scattering spectrum of the crystal field excitations (inset : zoom on the E < 1 meV range), (b) specific heat and (c) magnetic moment distribution, carried out for $H = 0.45$ K, T = 2 K and different standard shifts δ, from 0.001 up to 0.100 Å.

Quadrupolar interactions. Quadrupole interactions are obviously missing in the previous analysis, and are considered in what follows. The charge distribution within the 4f cloud involves the five quadrupolar moments :

$$O_{i,2,-2} = I_i^x I_i^y + I_i^y I_i^x$$

$$O_{i,2,-1} = \frac{1}{2}(I_i^y I_i^z + I_i^z I_i^y)$$

$$O_{i,2,0} = 3I_i^z I_i^z - I(I+1)$$

$$O_{i,2,1} = \frac{1}{2}(I_i^x I_i^z + I_i^z I_i^x)$$

$$O_{i,2,2} = I_i^x I_i^x - I_i^y I_i^y$$

and quadrupolar interactions in principle introduce a term $K_{i,j}^{\mu,\nu} O_{i,2,\mu} O_{j,2,\nu}$ in the Hamiltonian, hence $O_{2,m}$ terms which are otherwise forbidden. Detailed knowledge about the $K_{i,j}^{\mu,\nu}$ interactions is clearly beyond the scope of the present work. It is possible however, to bypass such a microscopic description of those quadrupolar interactions if one projects the full Hamiltonian onto the subspace spanned by the ↑ and ↓ states which form the degrees of freedom

of a pseudo spin ½ labelled σ_i. This projection will not reproduce high energy CF levels, but should provide insight into the low energy features.

The z component of this pseudo spin is directly related to the actual local magnetic moment $I_i^z = 2\,\mu\,\sigma_i^z$. This gives rise to a term

$$\sum_{<i,j>} J^{zz}\,\sigma_i^z\,\sigma_j^z \qquad (6)$$

with $J^{zz} = 4\,\mu^2\,\mathcal{g}^{zz}$.

As explained above, oxygen shifts introduce deviations out of the D_{3d} symmetry, hence $O_{n,m}$ operators. A direct calculation within the J = 6 manifold shows that most $O_{n,m}$ have matrix elements which connect ↑ and ↓. This corresponds to $\sigma_i^{x,y}$ operators. As a result, the projected Hamiltonian encompasses a second term:

$$\sum_i \delta h_\perp\,\sigma_i^x \qquad (7)$$

and $\delta h_\perp$ represents the net effect of these random deviations. It is worth mentioning that the Hamiltonian (6)+(7) has been used in theoretical studies of disorder [31], [32], $\delta h_\perp$ being considered as a "transverse" effective random field.

With regard to quadrupole-quadrupole interactions, since the quadrupolar $O_{2,m}$ operators also project onto σ_i^x and σ_j^y , quadrupolar interactions are expected to induce an effective coupling among and between σ_i^x and σ_j^y operators at neighboring sites. According to [53], [54], [55], [56], the corresponding Hamiltonian should involve two effective coupling constants $k^{\pm}$ and $k^{\pm\pm}$:

$$\mathcal{H'}_q = \sum_{<i,j>} -k^{\pm}\left(\sigma_i^+\,\sigma_j^- + \sigma_i^-\,\sigma_j^+\right) + k^{\pm\pm}\left(\gamma_{ij}\sigma_i^+\,\sigma_j^+ + \gamma_{ij}^*\sigma_i^-\,\sigma_j^-\right) \qquad (8)$$

At the mean field level, decoupling of the product of two operators entering $\mathcal{H'}_q$ will produce an effective transverse molecular field $\bar{h}_\perp$ acting on the *x* and *y* components of the pseudo spin, hence a term:

$$\sum_i \bar{h}_\perp \sigma_i^x$$

formally identical to (7). This means that $\mathcal{H'}_q$ can be incorporated into the model of Eq. (6)+(7), provided the transverse field is the sum of a constant value $\bar{h}_\perp$, describing the net result of quadrupolar interactions (at least in the mean-field approximation), and a random contribution

$\delta h_\perp$ associated with oxygen shifts, i.e, with the actual disorder. For the sake of simplicity, we shall now consider the mean field version of Hamiltonian (6)+(7)+(8):

$$\mathcal{H}' \approx \sum_i h\,\sigma_i^z + \sum_i h_\perp\,\sigma_i^x \quad (9)$$

$h = 2\mu H$ is the longitudinal molecular field, due to magnetic interactions, and $h_\perp = \left(\bar{h}_\perp + \delta h_\perp\right)$ is the transverse effective field. Diagonalization of Eq (9) shows that the eigenstates are $|1\rangle = \cos\theta\,|\uparrow\rangle + \sin\theta\,|\downarrow\rangle$ and $|2\rangle = \cos\theta\,|\uparrow\rangle - \sin\theta\,|\downarrow\rangle$, separated by $\Delta = \sqrt{h^2 + {h_\perp}^2}$, with :

$$\cos 2\theta = \frac{h}{\Delta} \quad \sin 2\theta = \frac{h_\perp}{\Delta}$$

At low temperature, the neutron spectrum writes :

$$S(\omega) \approx \mu^2/4\,\left\{\frac{h^2}{h^2+{h_\perp}^2}\,\delta(\omega) + \frac{{h_\perp}^2}{h^2+{h_\perp}^2}\,\delta(\omega-\Delta)\right\} \quad (10)$$

Again, in this expression, Δ and $h_\perp = \bar{h}_\perp + \delta h_\perp$ should be considered as random number, associated with a random configuration of the oxygen atoms. $S(\omega)$ contains two contributions, elastic and inelastic, with complementary spectral weights, reflecting the competition between the longitudinal (h) and transverse ($h_\perp$) fields: from Eq. (10), the molecular field h lifts the degeneracy between $\uparrow$ and $\downarrow$, yielding a finite Δ, but the spectral weight of the peak at Δ is *vanishingly small*. A significant intensity is only restored if the transverse term $h_\perp$ is large enough. This fairly simple formulation thus provides a physical understanding of the nature of the low-energy peak reported in Figure 8a, especially the behavior of its intensity as a function of disorder strength.

Finally, it is instructive to compare the disorder strength to the effective magnetic coupling. We first consider $\bar{h}_\perp = 0$. The transverse field is then a result of positional disorder only, that is $h_\perp = \delta h_\perp$. Using the experimental values determined earlier, we deduce $\Delta = 0.37$ meV $\approx h$ and $\Gamma = 0.25$ meV $\approx \delta h_\perp$. Furthermore, at the mean field level, (6) becomes: $h\,\sigma_i^z = \left(\sum_j J^{zz}\,\langle\sigma_j^z\rangle\right)\,\sigma_i^z$; assuming 2-in 2-out configurations, $h = \sum_j J^{zz}\,\langle\sigma_j^z\rangle = 2\,J^{zz}\frac{1}{2} = J^{zz}$. We can then estimate:

$$h \approx J^{zz} \approx 4.3\,K, \qquad \delta h_\perp \approx 2.9\,K, \qquad \frac{\delta h_\perp}{J^{zz}} \sim 0.67.$$

We now take into account the quadrupolar term ($\bar{h}_\perp \neq 0$) and use: $\Delta = 0.37$ meV $\approx \sqrt{h^2 + \bar{h}_\perp{}^2}$, $\Gamma = 0.25$ meV $\approx \delta h_\perp$. To determine h, we propose to use the expression of the magnetic moment $M_z = 2\, g_J\, \mu\, (\frac{1}{2}\cos 2\theta) = g_J\, \mu\, \frac{h}{\Delta}$, that we shall identify with the (nearest neighbor) "correlated moment" $\sqrt{\rho_1} = 6$ μ_B (and not with $\sqrt{\rho_o}$, as it is not a direct result of correlations). With this assumption, we now obtain:

$$h \approx J^{zz} \approx 3.7\ K, \qquad \bar{h}_\perp \approx 2.2\ K, \qquad \delta h_\perp \approx 2.9\ K$$

hence

$$\frac{\delta h_\perp}{J^{zz}} \sim 0.8, \quad \frac{\bar{h}_\perp}{J^{zz}} \sim 0.6$$

This analysis suggests that disorder and quadrupolar effects are of the same order of magnitude in TbMOX. These values can be further discussed in a broader perspective, based on recent theoretical works [32], [31], [57]. From their solution for Eq. (6)+(7), the authors determined a $\bar{h}_\perp$ vs $\delta h_\perp$ phase diagram that is reproduced schematically in Figure 9. The classical spin ice is restricted to $\bar{h}_\perp = \delta h_\perp = 0$ and evolves towards a U(1) Quantum Spin Liquid (QSL) for finite $\bar{h}_\perp$. These studies argue that the latter withstands large $\bar{h}_\perp$ but eventually gives way to a "polarized" phase beyond a certain threshold $\frac{\bar{h}_\perp}{J^{zz}} \gtrsim 0.60$. In this polarized phase, the pseudo spin points along the x-axis, indicating that this is a quadrupolar phase in nature. The ratio of $\frac{\bar{h}_\perp}{J^{zz}} \sim 0.6$ obtained in TbMOX, even if it should be considered with care, would locate the latter close to the border between the QSL and polarized phase, hence very far from the classical spin ice. At lower $\bar{h}_\perp$, however, these theoretical works present results that appear contradictory. While the QSL firmly resists $\delta h_\perp$ according to refs. [31], [32], ref. [57] predicts another instability. This transition line behaves as $\delta h_\perp \approx 0.9\, \bar{h}_\perp{}^2$. Beyond this line, the system enters a succession of glassy phases, first a disordered Ising phase (I) and eventually at even larger $\delta h_\perp$ a Griffiths-McCoy phase (GMC). According to these studies, the Ising phase is characterized by the lifting of degeneracy within the spin-ice manifold, whereas the Griffiths-McCoy phase is characterized by rare pockets where the entanglement typical of QSL is preserved. With all precautions coming along with the estimations presented above, $\frac{\delta h_\perp}{J^{zz}} \sim 0.7 - 0.8$ locates TbMox in the latter phase.

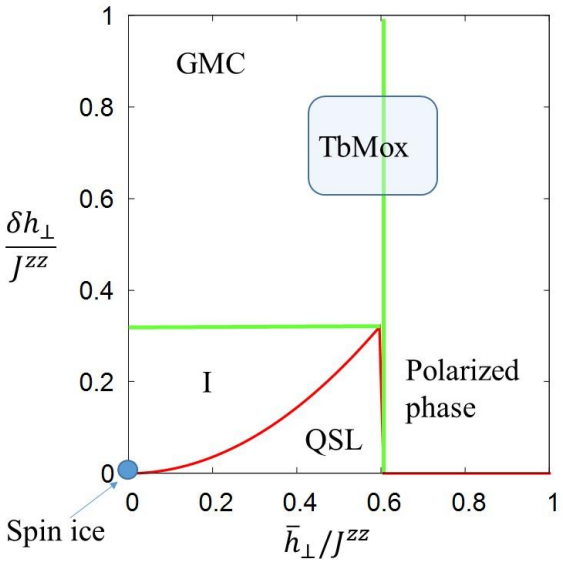

Figure 9. Schematic phase diagram constructed based on the theoretical results discussed in Refs. [32] and [57]. The green line depicts the transition to the polarized phase and/or Griffiths-McCoy, the red line to the glassy Ising state (I). GMC is the Griffiths-McCoy phase described in the text. The classical spin ice appears at $\bar{h}_\perp = \delta h_\perp = 0$. The light blue rectangle shows the estimated TbMox location.

DISCUSSION

The impact of inherent disorder in the entropy-stabilized pyrochlore $Tb_2(TiZrHfGeSn)_2O_7$ studied here can be reasonably well understood based on random positional shifts δ of the oxygen ions surrounding Tb^{3+}. As expected, disorder first causes a broadening of the high energy crystal field excitations of Tb^{3+}. In both disordered pyrochlores $Tb_2Hf_2O_7$ and Tb_2ScNbO_7, very similar broad CF levels have been observed around 4.5, 17 and 35 meV, and also interpreted (in the case of Tb_2ScNbO_7) using a distributed point charge model. However, the most striking effect of positional disorder is its contribution to the spectral weight of the low energy CF mode. Our modeling clearly shows that the spectral weight of this low energy mode systematically originates from a deviation from the D_{3d} symmetry, with two possible physical origins for this deviation, either disorder and/or quadrupolar interactions. Because the presence of such a low energy mode in neutron scattering spectra is actually a common feature in a number of Tb based pyrochlores, disordered or not, like $Tb_2Ti_2O_7$, $Tb_2Sn_2O_7$, $Tb_2Ge_2O_7$, $Tb_2Nb_2O_7$ [58], $Tb_2Hf_2O_7$ and Tb_2ScNbO_7 [19] [59, 52, 37, 37], the question that naturally arises then is how to ponder the relative contributions of both effects in these compounds.

In disordered TbMOX, both disorder and quadrupolar effects seem to be of the same order of magnitude, as estimated from $\frac{\delta h_\perp}{J^{zz}}$ and $\frac{\bar{h}_\perp}{J^{zz}}$, posing it as a glassy phase. This would be consistent

with experimental findings, as the frequency dependence of the magnetic susceptibility is akin to that of a spin glass. It is also of interest to use the parameters presented earlier, that is the values of Δ, Γ and of the local moment, to place compounds as $Tb_2Hf_2O_7$ [37] and Tb_2ScNbO_7 [36], in this phase diagram. In particular, in Tb_2ScNbO_7, it seems that disorder is so strong (from a visual estimate of Γ ~ 1 meV), that this compound most certainly lies deeper in the Griffiths phase. This would also be consistent with the frequency dependence of its magnetic susceptibility.

This point is all the more interesting that TbMOX is *a priori* much more disordered than Tb_2ScNbO_7, since cationic sizes vary from 0.53 Å to 0.72 Å, while Sc^{3+} and Nb^{5+} have similar sizes (0.745 Å and 0.72 Å, respectively). However, the random distribution of 3+ and 5+ charges also has a significant impact on the ground state CF level, and it is very likely that this is the main reason why Tb_2ScNbO_7 looks more disordered, in terms of its impact on the CF levels, than TbMOX. In the latter material, the homogeneity of the 4+ charge carried by the cations smoothens out the disorder.

The MOX approach then appears as a way to move around the phase diagram of Figure 9 : control of the transverse field distribution could be achieved by varying experimental parameters during the synthesis procedure, hence navigating between transition lines in the phase diagram.

In disorder free compounds like $Tb_2Ti_2O_7$, one should expect quadrupolar interactions to be the only relevant parameter ($h_\perp = \bar{h}_\perp$). In $Tb_2Ti_2O_7$, there is actually abundance of experimental evidence that quadrupolar interactions are at play. The fact that the low energy mode at Δ is dispersing is also a good indication that those interactions provide the stiffness necessary to propagate such collective excitations. This compound is also intrinsically sensitive to defects, as evidenced by the existence of a long range quadrupolar phase in $Tb_{2+x}Ti_{2-x}O_{7+y}$ for x = 0.005. The subtle perturbation introduced by disorder is enough to unbalance the ground state towards an ordered phase, so that the scenario that emerges is that $Tb_2Ti_2O_7$ is close to a boundary between an exotic disordered state and this ordered quadrupolar phase. In the phase diagram of Figure 9, $Tb_2Ti_2O_7$ could therefore be placed close to the boundary between QSL and the polarized phase, keeping $\frac{\delta h_\perp}{J^{zz}} = 0$.

Note here that $Tb_2Sn_2O_7$ and $Tb_2Ge_2O_7$ have their own specificity, as they both order at low temperature in a long range ordered “canted spin ice” ground state, which testifies of

ferromagnetic interactions. Recent exhaustive work on $Tb_2Ge_2O_7$ proposes that quadrupole-quadrupole interactions could be also at the origin of the large spectral weight of the low energy mode [52], in agreement with our conclusions.

CONCLUSION

This comprehensive study of the entropy-stabilized terbium pyrochlore $Tb_2(TiZrHfGeSn)_2O_7$ points out several similarities with parent $Tb_2Ti_2O_7$, including antiferromagnetic interactions between nearest neighbours, and the presence at low energy (0.4 meV) of a nearly flat inelastic mode, whose energy width remains quite narrow despite the intrinsic chemical disorder. Those experimental observations are understood based on a scenario in which compositional disorder translates into random shifts of the oxygen atoms. Numerical calculations show that the Tb magnetic moment amplitude is not strongly affected by disorder, and that oxygen shifts broaden the high energy CF levels considerably and contribute to the intensity of the low energy mode. More generally, this scenario offers a better understanding of the effect of disorder, quadrupolar interactions and antiferromagnetic exchange on the ground state of Tb pyrochlores. Based on this scenario, as it provides a tunable and rather smooth disorder, the high entropy approach offers promising perspectives to achieve QSL phases in Tb, and more generally non-Kramers rare-earths, pyrochlores.

ACKNOWLEDGEMENTS

This work was partially supported by the ANR Fragment (ANR 19-CE30-0040), and ANR NEO (ANR 19-CE30-0030-01). Part of this work is based on experiments performed at the Swiss spallation neutron source SINQ, Paul Scherrer Institute, Villigen, Switzerland, which were financially supported by the Fédération Française de la Neutronique (2FDN). SP acknowledges A. Roll for fruitful discussions, SP and FD also thank O. Benton for most enlightening explanations. FV thanks the École Normale Supérieure (ENS) Paris-Saclay for her Ph.D. funding.

Data availibility statement

All the data supporting the findings of this study, including the raw data generated at the ILL and SINQ large-scale facilities are available from the corresponding author upon reasonable request.

REFERENCES

[1] F. VAYER, C. DECORSE, D. BERARDAN, D. DRAGOE, and N. DRAGOE, *Journal of the American ceramicOF THE AMERICAN CERAMIC SOCIETY* **106**, 2601 (2023).

[2] F. VAYER, C. DECORSE, D. BERARDAN, and N. DRAGOE, *Journal of Alloys and Compounds* **883**, 160773 (2021).

[3] C. M. ROST, E. SACHET, T. BORMAN, A. MOBALLEGH, E. C. DICKEY, D. HOU, J. L. JONES, S. CURTAROLO, and J. P. MARIA, *Nature Communications* **6**, 8485 (2015).

[4] R. Z. ZHANG, F. GUCCI, H. Y. ZHU, K. CHEN, and M. J. REECE, *Inorganic Chemistry* **57**, 13027 (2018).

[5] T. A. A. BATCHELOR, J. K. PEDERSEN, S. H. WINTHER, I. E. CASTELLI, K. W. JACOBSEN, and J. ROSSMEISL, *Joule* **3**, 834 (2019).

[6] D. BERARDAN, S. FRANGER, D. DRAGOE, A. K. MEENA, and N. DRAGOE, *physica status solidi (RRL) â€“ Rapid Research Letters* **10**, 328 (2016).

[7] A. SARKAR, L. VELASCO, D. WANG, Q. S. WANG, G. TALASILA, L. DE BIASI, C. KUBEL, T. BREZESINSKI, S. S. BHATTACHARYA, H. HAHN, and B. BREITUNG, *Nature Communications* **9**, 3400 (2018).

[8] C. LACROIX, P. MENDELS, and F. MILA, editors, *Introduction to Frustrated Magnetism*, Springer-Verlag, Berlin, 2011.

[9] J. S. GARDNER, M. J. P. GINGRAS, and J. E. GREEDAN, *Rev. Mod. Phys.* **82** (2010).

[10] M. J. P. GINGRAS and P. A. MCCLARTY, *Reports on Progress in Physics* **77**, 056501 (2014).

[11] J. S. GARDNER, S. R. DUNSIGER, B. D. GAULIN, M. J. P. GINGRAS, J. E. GREEDAN, R. F. KIEFL, M. D. LUMSDEN, W. A. MACFARLANE, N. P. RAJU, J. E. SONIER, I. SWAINSON, and Z. TUN, *Phys. Rev. Lett.* **82**, 1012 (1999).

[12] M. J. HARRIS, S. T. BRAMWELL, P. C. W. HOLDSWORTH, and J. D. M. CHAMPION, *Phys. Rev. Lett.* **81**, 4496 (1998).

[13] A. P. RAMIREZ, A. HAYASHI, R. J. CAVA, R. SIDDHARTHAN, and B. S. SHASTRY, *Nature* **399**, 333 (1999).

[14] S. T. BRAMWELL and M. J. P. GINGRAS, *Science* **294**, 1495 (2001).

[15] T. FENNELL, P. P. DEEN, A. R. WILDES, K. SCHMALZL, D. PRABHAKARAN, A. T. BOOTHROYD, R. J. ALDUS, D. F. MCMORROW, and S. T. BRAMWELL, *Science* **326**, 415 (2009).

[16] S. H. CURNOE, *Phys. Rev. B* **78**, 094418 (2008).

[17] Y. CHAPUIS, A. YAOUANC, P. DALMAS DE RÉOTIER, C. MARIN, S. VANISHRI, S. H. CURNOE, C. VÂJU, and A. FORGET, *Phys. Rev. B* **82**, 100402 (2010).

[18] P. BONVILLE, I. MIREBEAU, A. GUKASOV, S. PETIT, and J. ROBERT, *Phys. Rev. B* **84**, 184409 (2011).

[19] S. PETIT, P. BONVILLE, J. ROBERT, C. DECORSE, and I. MIREBEAU, *Physical Review B* **86**, 174403 (2012).

[20] S. GUITTENY, J. ROBERT, P. BONVILLE, J. OLLIVIER, C. DECORSE, P. STEFFENS, M. BOEHM, H. MUTKA, I. MIREBEAU, and S. PETIT, *Phys. Rev. Lett.* **111**, 087201 (2013).

[21] P. BONVILLE, A. GUKASOV, I. MIREBEAU, and S. PETIT, *Phys. Rev. B* **89**, 085115 (2014).

[22] T. FENNELL, M. KENZELMANN, B. ROESSLI, H. MUTKA, J. OLLIVIER, M. RUMINY, U. STUHR, O. ZAHARKO, L. BOVO, A. CERVELLINO, M. K. HAAS, and R. J. CAVA, *Physical Review Letters* **112**, 017203 (2014).

[23] M. RUMINY, S. GUITTENY, J. ROBERT, L.-P. REGNAULT, M. BOEHM, P. STEFFENS, H. MUTKA, J. OLLIVIER, U. STUHR, J. S. WHITE, B. ROESSLI, L. BOVO, C. DECORSE, M. K. HAAS, R. J. CAVA, I. MIREBEAU, M. KENZELMANN, S. PETIT, and T. FENNELL, *Physical Review B* **99**, 224431 (2019).

[24] H. TAKATSU, S. ONODA, S. KITTAKA, A. KASAHARA, Y. KONO, T. SAKAKIBARA, Y. KATO, B. FÅK, J. OLLIVIER, J. W. LYNN, T. TANIGUCHI, M. WAKITA, and H. KADOWAKI, *Phys. Rev. Lett.* **116**, 217201 (2016).

[25] H. KADOWAKI, M. WAKITA, B. FÃ¥K, J. OLLIVIER, S. OHIRA-KAWAMURA, K. NAKAJIMA, H. TAKATSU, and M. TAMAI, *Journal of the Physical Society of Japan* **87**, 064704 (2018).

[26] T. TANIGUCHI, H. KADOWAKI, H. TAKATSU, B. FÅK, J. OLLIVIER, T. YAMAZAKI, T. J. SATO, H. YOSHIZAWA, Y. SHIMURA, T. SAKAKIBARA, T. HONG, K. GOTO, L. R. YARASKAVITCH, and J. B. KYCIA, *Phys. Rev. B* **87**, 060408 (2013).

[27] N. MARTIN, P. BONVILLE, E. LHOTEL, S. GUITTENY, A. WILDES, C. DECORSE, M. CIOMAGA HATNEAN, G. BALAKRISHNAN, I. MIREBEAU, and S. PETIT, *Phys. Rev. X* **7**, 041028 (2017).

[28] J.-J. WEN, S. M. KOOHPAYEH, K. A. ROSS, B. A. TRUMP, T. M. MCQUEEN, K. KIMURA, S. NAKATSUJI, Y. QIU, D. M. PAJEROWSKI, J. R. D. COPLEY, and C. L. BROHOLM, *Phys. Rev. Lett.* **118**, 107206 (2017).

[29] R. SIBILLE, E. LHOTEL, M. C. HATNEAN, G. BALAKRISHNAN, B. FÅK, N. GAUTHIER, T. FENNELL, and M. KENZELMANN, *Phys. Rev. B* **94**, 024436 (2016).

[30] R. SIBILLE, N. GAUTHIER, H. YAN, M. CIOMAGA HATNEAN, J. OLLIVIER, B. WINN, G. BALAKRISHNAN, M. KENZELMANN, N. SHANNON, and T. FENNELL, *Nature Phys.* **14**, 711 (2018).

[31] L. SAVARY and L. BALENTS, *Phys. Rev. Lett.* **118**, 087203 (2017).

[32] O. BENTON, *Phys. Rev. Lett.* **121**, 037203 (2018).

[33] S. V. ISAKOV, K. GREGOR, R. MOESSNER, and S. L. SONDHI, *Physical Review Letters* **93**, 167204 (2004).

[34] C. L. HENLEY, *Physical Review B* **71**, 014424 (2005).

[35] C. L. HENLEY, *Annual Review of Condensed Matter Physics* **1**, 179 (2010).

[36] Y. ALEXANIAN, E. LHOTEL, R. BALLOU, C. V. COLIN, H. KLEIN, A. LE PRIOL, F. MUSEUR, J. ROBERT, E. PACHOUD, P. LEJAY, A. HADJ-AZZEM, B. FÅK, Q. BERROD, J.-M. ZANOTTI, E. SUARD, C. DEJOIE, S. DE BRION, and V. SIMONET, *Phys. Rev. Mater.* **7**, 094403 (2023).

[37] R. Sibille, E. Lhotel, M. Ciomaga Hatnean, G. J. Nilsen, G. Ehlers, A. Cervellino, E. Ressouche, M. Frontzek, O. Zaharko, V. Pomjakushin, U. Stuhr, H. C. Walker, D. T. Adroja, H. Luetkens, C. Baines, A. Amato, G. Balakrishnan, T. Fennell, and M. Kenzelmann, *Nature Communications* **8**, 892 (2017).

[38] L. T. Denisova, L. A. Irtyugo, Y. F. Kargin, V. V. Beletskii, and V. M. Denisov, *Inorganic Materials* **53**, 93 (2017).

[39] L. T. Denisova, L. A. Irtyugo, Y. F. Kargin, V. M. Denisov, and V. V. Beletskii, *Russian Journal of Inorganic Chemistry* **62**, 814 (2017).

[40] J. Rodriguez-Carvajal, *Physica B* **192**, 55 (1993).

[41] J. Mesot, S. Janssen, L. Holitzner, and R. Hempelmann, *Journal of Neutron Research* **3**, 293 (1996).

[42] C. A. Catanese, A. T. Skjeltorp, H. E. Meissner, and W. P. Wolf, *Phys. Rev. B* **8**, 4223 (1973).

[43] N. Hamaguchi, T. Matsushita, N. Wada, Y. Yasui, and M. Sato, *Physical Review B* **69** (2004).

[44] V. F. Sears, *Neutron News* **3**, 26 (1992).

[45] K. Matsuhira, Y. Hinatsu, K. Tenya, H. Amitsuka, and T. Sakakibara, *JOURNAL OF THE PHYSICAL SOCIETY OF JAPAN* **71**, 1576 (2002).

[46] V. K. Anand, L. Opherden, J. Xu, D. T. Adroja, A. D. Hillier, P. K. Biswas, T. Herrmannsdoerfer, M. Uhlarz, J. Hornung, J. Wosnitza, E. Canevet, and B. Lake, *PHYSICAL REVIEW B* **97** (2018).

[47] M. J. P. Gingras, B. C. den Hertog, M. Faucher, J. S. Gardner, S. R. Dunsiger, L. J. Chang, B. D. Gaulin, N. P. Raju, and J. E. Greedan, *Phys. Rev. B* **62**, 6496 (2000).

[48] I. Mirebeau, P. Bonville, and M. Hennion, *Phys. Rev. B* **76**, 184436 (2007).

[49] E. Lhotel, C. Paulsen, P. D. de Réotier, A. Yaouanc, C. Marin, and S. Vanishri, *Phys. Rev. B* **86**, 020410 (2012).

[50] Y. CHAPUIS, *Frustration géométrique, transitions de phase et ordre dynamique, Thèse de Doctorat*, PhD thesis, Université Joseph Fourier, 2009.

[51] K. A. ROSS, L. SAVARY, B. D. GAULIN, and L. BALENTS, *Phys. Rev. X* **1**, 021002 (2011).

[52] A. M. HALLAS, W. JIN, J. GAUDET, E. M. TONITA, D. POMARANSKI, C. R. C. BUHARIWALLA, M. TACHIBANA, N. P. BUTCH, S. CALDER, M. B. STONE, G. M. LUKE, C. R. WIEBE, J. B. KYCIA, M. J. P. GINGRAS, and B. D. GAULIN, Intertwined Magnetic Dipolar and Electric Quadrupolar Correlations in the Pyrochlore $Tb_2Ge_2O_7$, 2020.

[53] L. SAVARY and L. BALENTS, *Phys. Rev. Lett.* **108**, 037202 (2012).

[54] S. LEE, S. ONODA, and L. BALENTS, *Phys. Rev. B* **86**, 104412 (2012).

[55] S. ONODA and Y. TANAKA, *Phys. Rev. Lett.* **105**, 047201 (2010).

[56] S. ONODA and Y. TANAKA, *Phys. Rev. B* **83**, 094411 (2011).

[57] T. PARDINI, A. MENON, S. P. HAU-RIEGE, and R. R. P. SINGH, *Phys. Rev. B* **100**, 144437 (2019).

[58] Y. M. JANA, O. SAKAI, R. HIGASHINAKA, H. FUKAZAWA, Y. MAENO, P. DASGUPTA, and D. GHOSH, *Phys. Rev. B* **68**, 174413 (2003).

[59] S. PETIT, P. BONVILLE, I. MIREBEAU, H. MUTKA, and J. ROBERT, *Phys. Rev. B* **85**, 054428 (2012).